

Supporting Information

A novel tandem reactor design based on nano-Cu electrocatalysts and microbial biocatalysts for converting CO₂ into ethylene and acetate

Juan Liu, Xiaoxiao Guo, Zhaoyuan Lyu, Rong-Bin Song, Pengyu Zhou, Shichao Ding, Yang Zhou, Li-Ping Jiang, Yuehe Lin*, and Wenlei Zhu*

1. Supplementary Figures

Fig. S1 Wood-Ljungdahl pathway in *M. thermoacetica*

Fig. S2 SEM image of *M. thermoacetica*

Fig. S3 Growth profiles of *M. thermoacetica* with glucose as carbon source

Fig. S4 Growth profiles of *M. thermoacetica* with HCOOH, CO, H₂, and CO₂ as the energy and carbon sources

Fig. S5 ¹H-NMR spectra of yeast extract

Fig. S6 Metabolic process of HCOOH when the yeast extract was removed

Fig. S7 Schematic diagram of the testing method for gas analysis

Fig. S8 I-t curve when *M. thermoacetica* accepts cathode electrons to electro-synthesize acetate

Fig. S9 A schematic illustration for the synthesis process of nano-copper electrocatalyst

Fig. S10 Size distribution of Cu(OH)₂

Fig. S11 Size distribution of CuO

Fig. S12 HRTEM image of CuO

Fig. S13 N₂ adsorption isotherms and pore size of CuO

Fig. S14 CO₂ adsorption curves of CuO

Fig. S15 SEM image and EDX maps of the CuO catalyst on GDL after in situ reduction

Fig. S16 HRTEM image of the CuO catalyst after in situ reduction

Fig. S17 Raman spectroscopy of the CuO catalyst after in situ reduction

Fig. S18 XRD patterns of a GDL and the cathode after electrocatalysis

Fig. S19 XPS spectra and Cu LMM Auger spectra of the catalyst

Fig. S20 LSV curves

Fig. S21 The stability of the electrocatalyst

Fig. S22 The tested pH value of catholyte after electrolysis at varied current densities

Fig. S23 Nyquist plots

Fig. S24 Tafel curve

Fig. S25 Operando Raman spectroscopy of the electrocatalysts/GDL

Fig. S26 D-band centers

Fig. S27 Schematic diagram of the tandem reactor

Fig. S28 A photograph of the experimental setup

Fig. S29 The ¹H-NMR spectra for the catholyte before and after the tandem experiments

Fig. S30 $^1\text{H-NMR}$ spectra of acetate labeled with ^{13}C

Fig. S31 SEM image and EDX maps of the microbe after the tandem experiment

Fig. S32 The activity of microbes after the tandem experiment

2. Supplementary Tables

Table S1. Medium

Table S2. Vitamin solution.

Table S3. Mineral Solution

Table S4. Rate of electron conversion to products by MES in a neutral electrolyte

Table S5. Rate of electron conversion to products by ECR in a neutral electrolyte

Table S6. Rate of electron conversion to products by tandem ECR in a neutral electrolyte

Medium. Nitriloacetic acid was purchased from Bide Pharmatech Ltd. Pyridoxine hydrochloride and Thiamine-HCl were bought from Aladdin Reagent (Shanghai) Co., Ltd. Nicotinic acid, thiocetic acid, vitamin B₁₂, and potassium formate were obtained from Shanghai Macklin Biochemical Co., Ltd. Calcium D-(+)-pantothenate, biotin, cysteine hydrochloride and resazurin sodium salt were purchased from Shanghai yuanye Bio-Technology Co., Ltd. Yeast extract was obtained from Qingdao Haibo Biotechnology Co., Ltd. All other reagents were obtained from Sinopharm Chemical Reagent Co., Ltd.

Reagents. Copper nitrate, sodium hydroxide, and potassium bicarbonate (KCl) were purchased from Shanghai Macklin Biochemical Co., Ltd. All chemicals were used as received. Nitrogen (99.5%), carbon dioxide (99.99%), carbon monoxide (99.99%), and hydrogen (99.99%) were purchased from Tianze gas, Inc. Deionized water from a Millipore Auto pure system was used as the solvent.

Flow cell electrolysis. Electrochemical measurements were conducted using an Autolab potentiostat (MAC 90177) in a three-electrode system. The reference electrode used was

Ag/AgCl (3 M KCl). The carbon paper with a microporous layer (Sigracet 29 BC, Fuel Cell Store) was used as the gas diffusion layer for supporting the catalyst, collecting the current, and acting as a pathway for gas from flow channels to the catalyst surface. The counter electrode used was the IrO₂-coated GDL (loading: 0.5 mg.cm⁻²). The working electrode was the Nanoporous-Cu-coated GDL. The catalyst-coated electrodes were prepared by hand-painting the catalyst ink, as previously reported. The catalyst ink consisted of 25 mg of catalyst ultrasonically dispersed in a mixture of 3 mL of n-propanol and 20 μL of Nafion (10 wt%) aqueous solution. (Fuel Cell Store). The mixture was then sonicated for 30 minutes. CO₂ electrolysis was carried out in a three-channel flow cell with channels of dimensions 2 × 0.5 × 0.15 cm³. The electrode area was 1 cm² and the distance between the electrode and membrane was 1.5 mm. An external Ag/AgCl reference electrode located ≈5 cm from the cathode was used to measure the cathodic half-cell potential. Poly(tetrafluoroethylene) (PTFE) gaskets were placed between each component for sealing and the device was tightened using six bolts. An external Ag/AgCl (3M KCl) acted as the reference electrode. And the electrochemical measurements were performed by an Autolab potential (204).

In addition, all the potentials were compensated by an Ir means and referred to as the RHE according to the formula:

$$E_{\text{RHE}} = E_{\text{Ag/AgCl}} + 0.197 \text{ V} + 0.059 \times \text{pH (in volts)}.$$

The pH values of the bulk electrolyte after electrolysis were used for RHE conversions unless stated otherwise. The gas flow rate into the flow cell was set at 10 sccm via a mass flow controller (Agilent Technologies, ADM 2000). The catholyte flow rates were controlled via a peristaltic pump (Baoding Chuangrui Pump Industry Co., Ltd), with a catholyte flow rate of 0.5 mL min⁻¹. The anolyte flow rate was 2 mL min⁻¹. An anion exchange membrane (FAA-3,

Fumatech) was used in the KCl electrolyte. Each reported data point reflects the mean of at least three measurements.

Gaseous product identification and quantification. The gaseous products were directed into the gas sampling loop of a GC (Agilent 7890B) for analysis. The GC was set up to split the gas sample into two aliquots. One aliquot was passed through a packed Mole Sieve 5A column and a packed HP-PLOT Q column before being detected by a thermal conductivity detector (TCD) for CO quantification. The other aliquot was routed through a packed HP-PLOT Q + PT column for the analysis of all major C₁ to C₃ hydrocarbons, which were detected by a flame ionization detector (FID) equipped with a methanizer (Agilent). The GC was calibrated using commercially available standards from JJS Technical Services. Nitrogen (Tianze, 99.99%) was used as the carrier gas. The faradaic efficiency (FE) for gas products was calculated using the following equation:

$$FE (\%) = \frac{i_x}{i_t} = \frac{e_x v_{gas} c_x F}{i_t V_m} \quad (1)$$

where i_x is the partial current of product x , i_t is the total current, e_x represents the number of electrons transferred towards the formation of 1 mol of product x , v_{gas} is the CO₂ flow rate (s.c.c.m), c_x represents the concentration of product x detected by gas chromatography (ppm), F is the Faraday constant (96485 C mol⁻¹), and V_m is the unit molar volume, which is 24.51 mol⁻¹ at room temperature (298.15K)

Liquid product identification and quantification. Liquid products were quantified using a Bruker DRX 400 Advance MHz spectrometer. Typically, 200 μL of the catholyte was mixed with 100 μL water and 200 μL sodium 3-(trimethylsilyl)-2,2',3,3'-tetradeuteropropionate (TMSP-d₄, Qingdao Tenglong Microwave Technology Co., Ltd) in D₂O (Acros Organics, 99.9

atom % D) as the internal standard. The 1D ^1H spectrum was measured with water suppression using a presaturation method. The Faradaic efficiency (FE) was calculated as follows:

$$\text{FE (\%)} = \frac{eFn}{Q} = \frac{eFn}{It} \quad (2)$$

where e is the number of electrons transferred, F is the Faraday constant, Q is the charge, I is current, t is the running time, and n is the total amount of product (in moles). Since

$$i = \frac{Q}{t} \quad i_x = i_t * FE_x = \frac{Q_x}{t} \quad (3)$$

$$g_x = \frac{i_x}{s} \quad (4)$$

$$v_x = \frac{n_x}{st} = \frac{Q_x}{ste_x} = \frac{I_x}{se_x} = \frac{g_x}{e_x} \quad (5)$$

Where i_x is the partial current of product x , i_t is the total current, Q_x and e_x represent the number of electrons transferred towards the formation of the total amount of product or 1 mol of product x (in moles), respectively. FE is the faradaic efficiency. s denotes the electrode area, and t means the time consumed for production. g_x is the current density. v_x is the production rate per unit electrode area per unit time in moles. The rate of electron conversion to products per unit electrode area per unit time, v_e , was calculated using the following equation:

$$v_e = v_x * e_x = \frac{g_x}{e_x} * e_x = g_x = \frac{i_t FE_x}{s} \quad (6)$$

FE_{liquid} is the total faradaic efficiency of liquid products. The faradaic selectivity (FS) of acetate was calculated as follows,

$$FS_{acetate} = \frac{FE_{acetate}}{FE_{liquid}} \quad (7)$$

Computational Methods: The partial density of states (PDOS) were calculated based on First-principles density functional theory (DFT). The Geometry Optimization of the system used CASTEP module.¹ The exchange-correlation effects were treated in generalized gradient approximation (GGA) with the Perdew-Burke-Ernzerhof (PBE) potential.² The kinetic energy cutoff was chosen to be 450 eV. Brillouin zone integration was accomplished using a 5×5×1 Monkhorst-Pack k-point mesh. The slabs were set by a vacuum region of 20 Å. The SCF tolerance is 1.0×10^{-5} eV atom⁻¹.

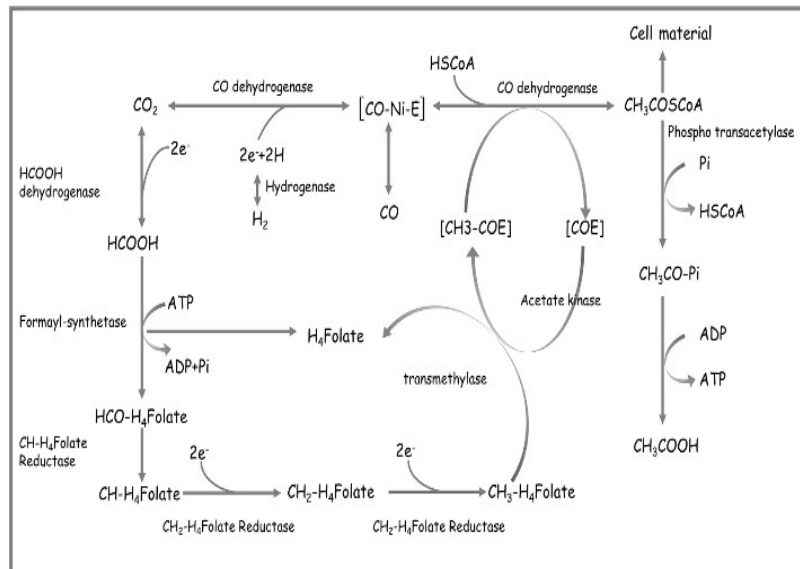


Fig. S1 The pathway of autotrophic fixation of CO₂ into acetyl coenzyme A for *Moorella thermoacetica*.

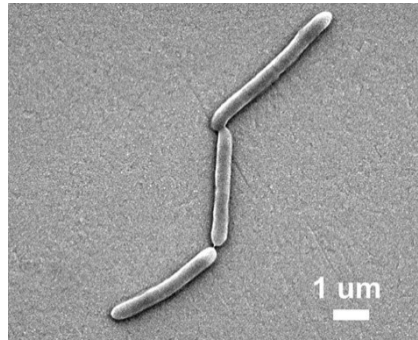


Fig. S2 SEM image of *M. thermoacetica*.

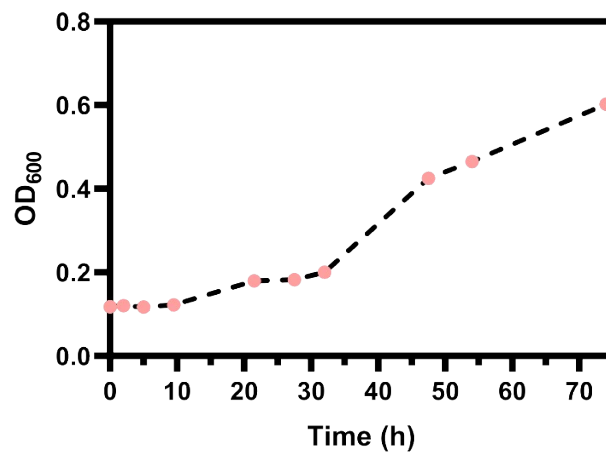


Fig. S3 The growth profiles of *M. thermoacetica* in the anaerobic tube with 8 g.L⁻¹ glucose as energy and carbon sources.

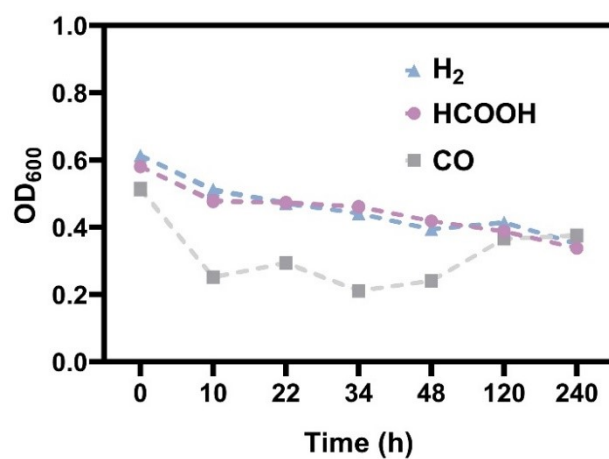


Fig. S4 The growth curve of *M. thermoacetica* in the anaerobic tube with HCOOH, CO, H₂, and CO₂ as the energy and carbon sources.

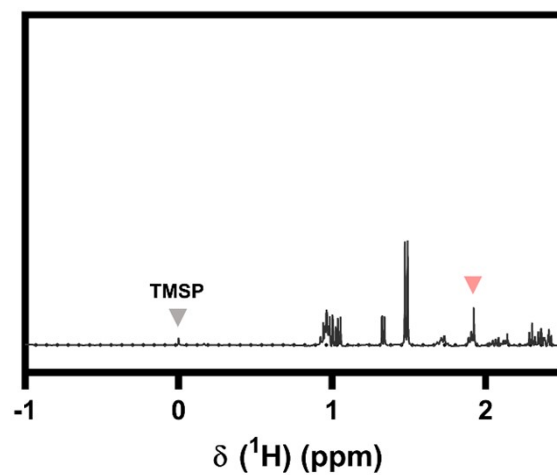


Fig. S5 ¹H-NMR spectra of the yeast extract in medium, displaying a peak at about 1.9 ppm chemical shift.

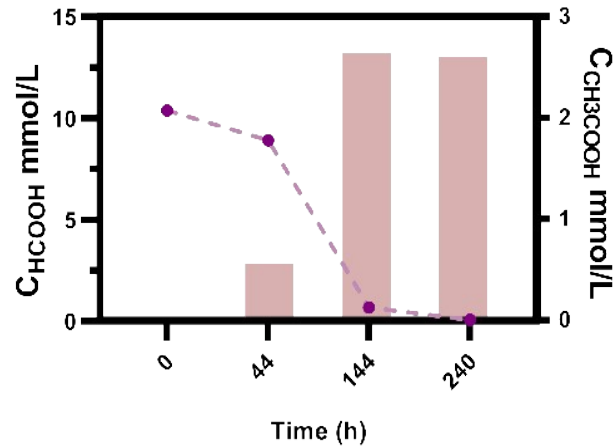


Fig. S6 The metabolic process of HCOOH when the yeast extract was removed. The content of HCOOH (line chart, left axis) was reduced, and the acetate concentration (histogram, right axis) increased to a constant value.

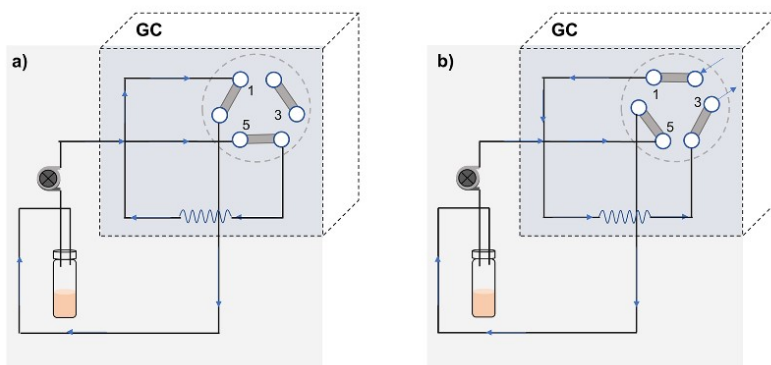


Fig. S7 Schematic diagram of the testing method for gas analysis. The gas in an anaerobic tube was squirmered into the gas chromatography and recycled back.

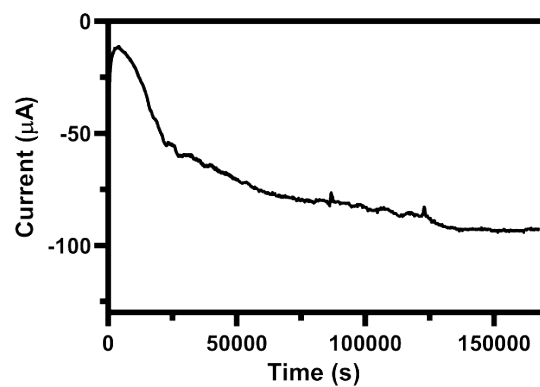


Fig. S8 I-t curve at a cathode potential of -0.4 V vs RHE, where acetate was synthesized by the microbes in the medium.

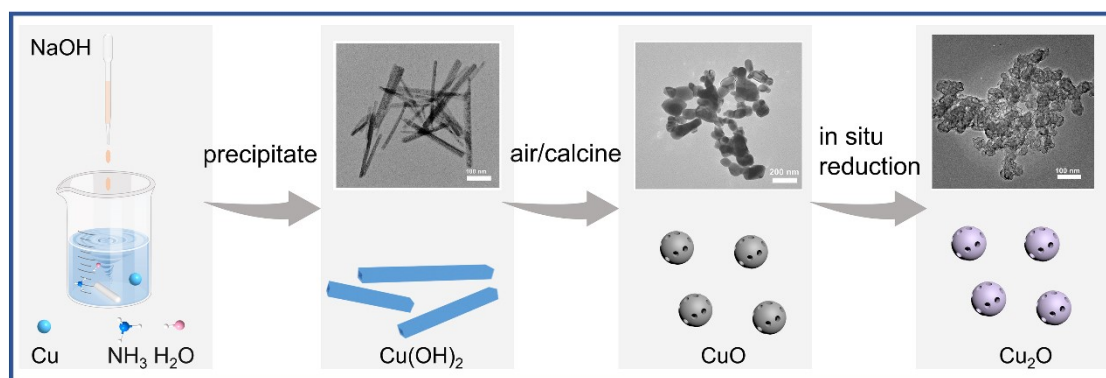


Fig. S9 A schematic illustration for the synthesis process of nano-copper electrocatalyst.

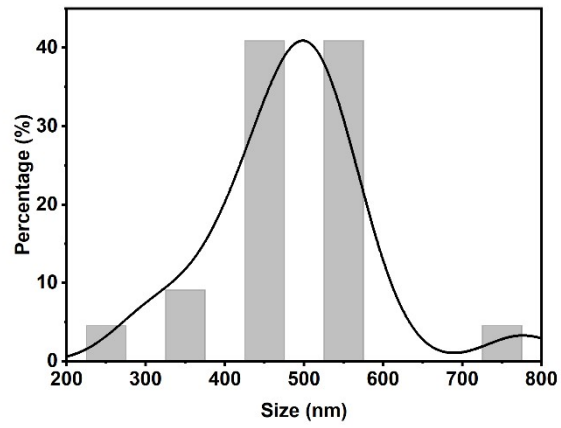


Fig. S10 The longitudinal size distribution of Cu(OH)₂.

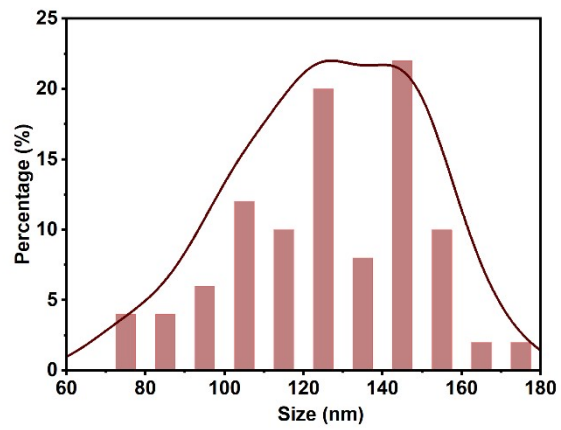


Fig. S11 The size distribution of CuO.

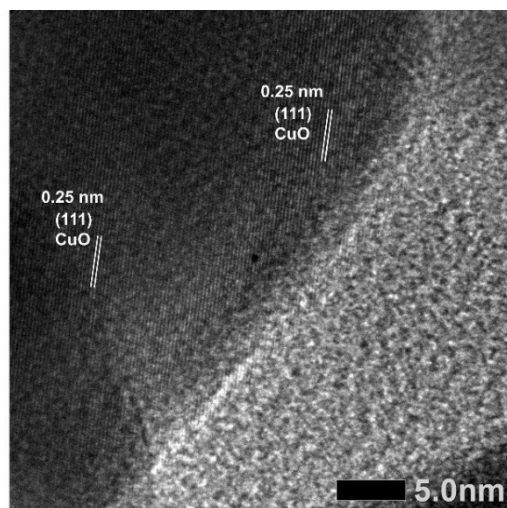


Fig. S12 HRTEM image of CuO.

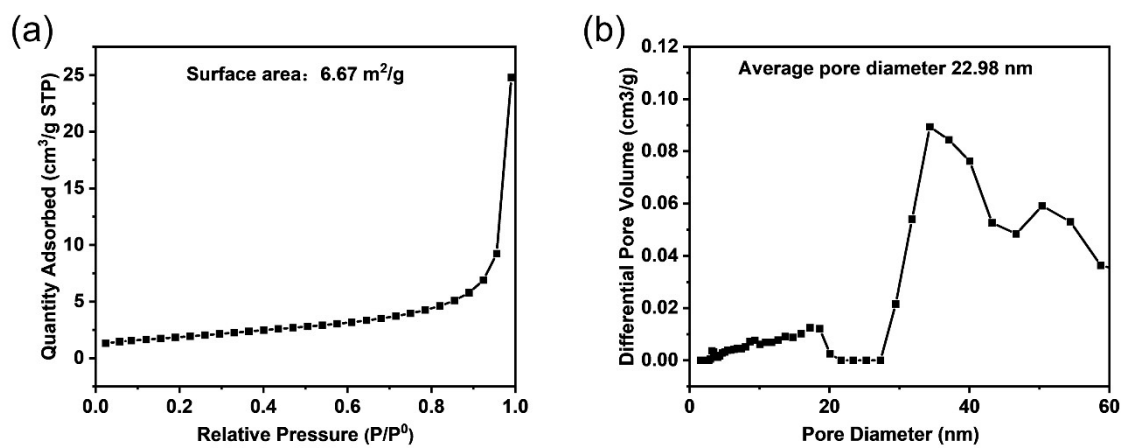


Fig. S13 N₂ adsorption isotherms of CuO (a) and its corresponding pore size distribution curve (b).

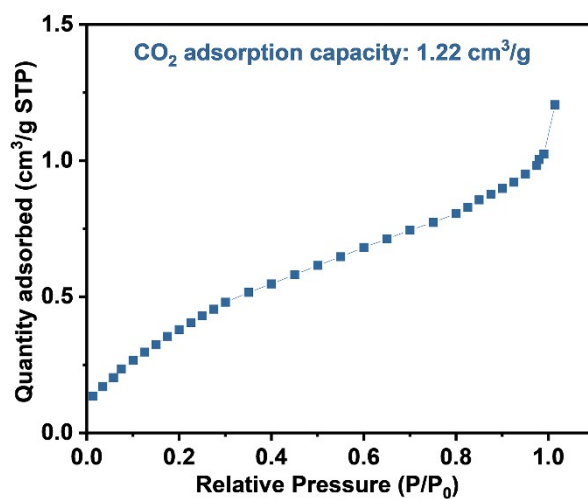


Fig. S14 CO₂ adsorption curves of CuO.

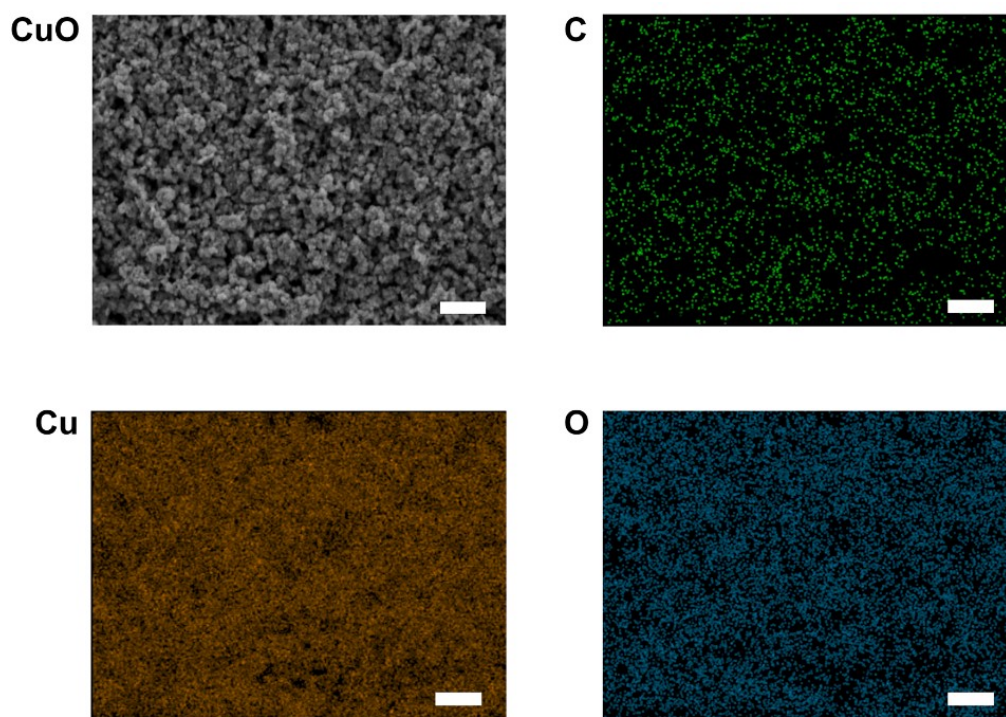


Fig. S15 The GDL cathode loaded with CuO electrocatalyst after in situ electroreduction. a) SEM image and EDX maps of the catalyst on GDL with uniform Cu and O distribution. All scale bars are 1000 nm.

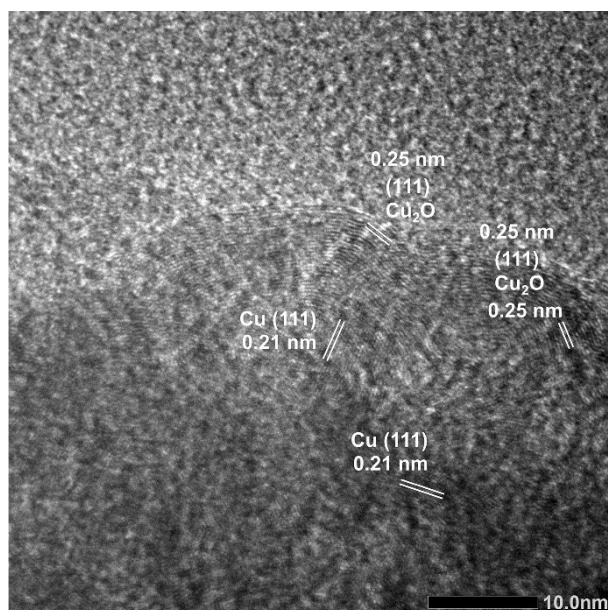
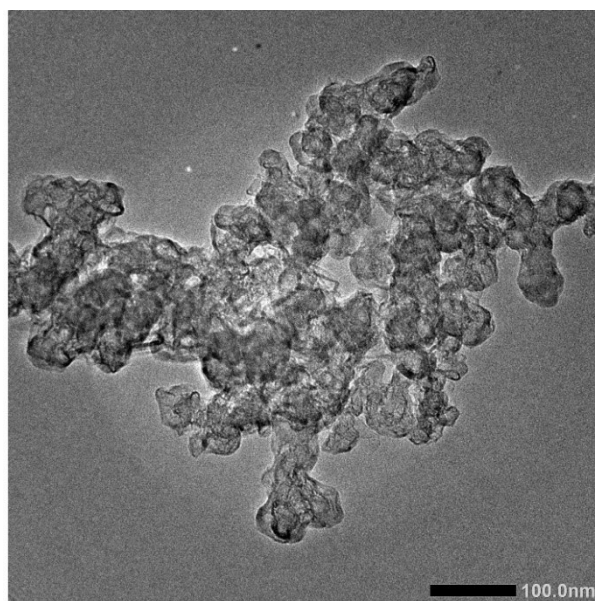


Fig. S16 HRTEM images of the CuO electrocatalyst after in situ electroreduction.

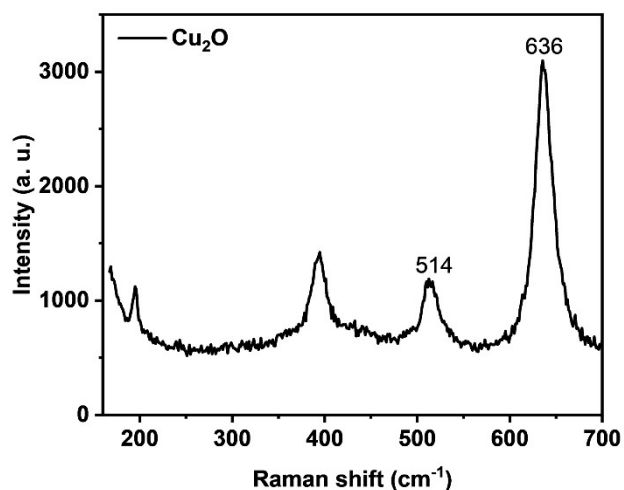


Fig. S17 Raman spectra of the CuO electrocatalyst after in situ electroreduction.

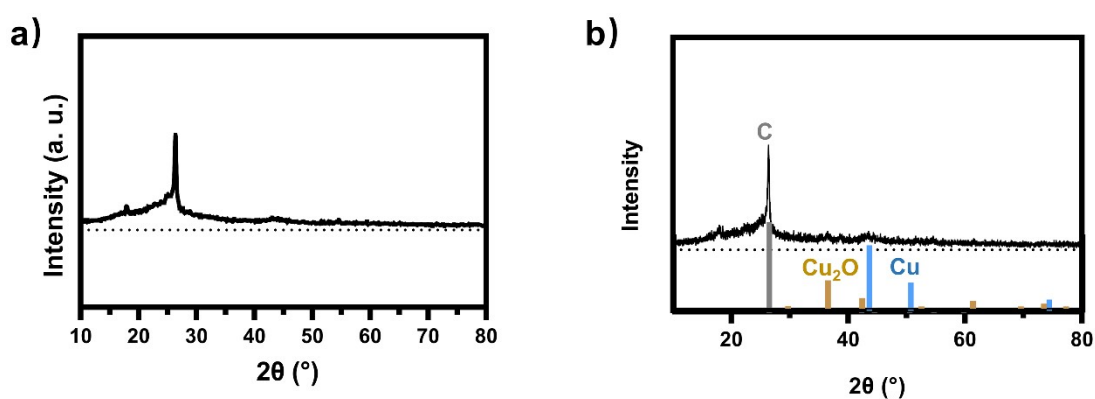


Fig. S18 a) XRD patterns of GDL or b) the nano-Cu cathode after electroreduction.

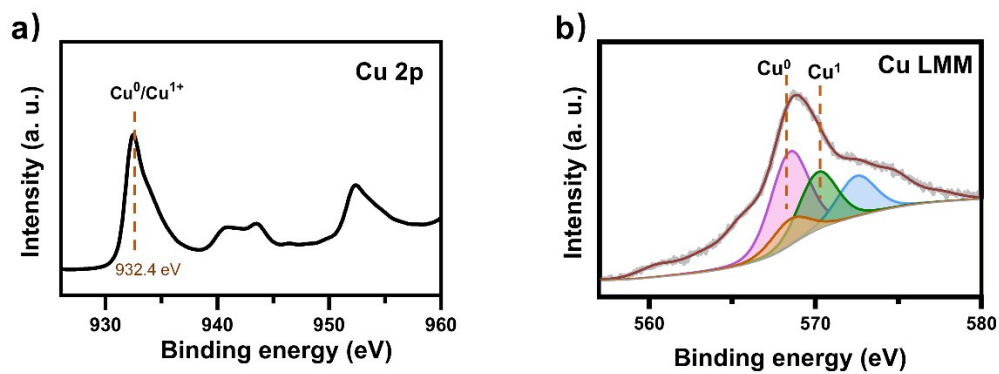


Fig. S19 a) Cu 2p XPS spectra and Cu LMM Auger spectra b) of the CuO catalyst after the electroreduction.

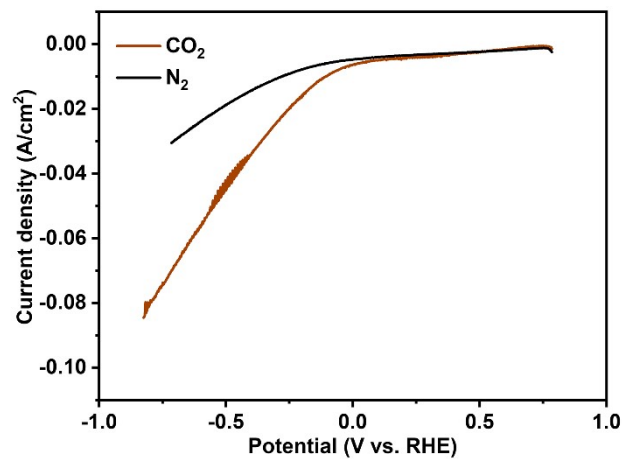


Fig. S20 LSV curves in 0.1 M KCl electrolytes with N₂ and CO₂ supplied from the gas chamber of the flow cell. (Scan rate: 5 mV s⁻¹)

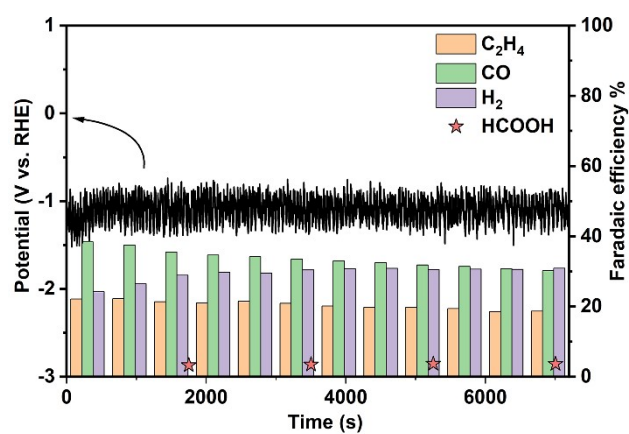


Fig. S21 The voltage profile and C₂H₄, CO, H₂, HCOOH FEs at a constant current density of 100 mA cm⁻².

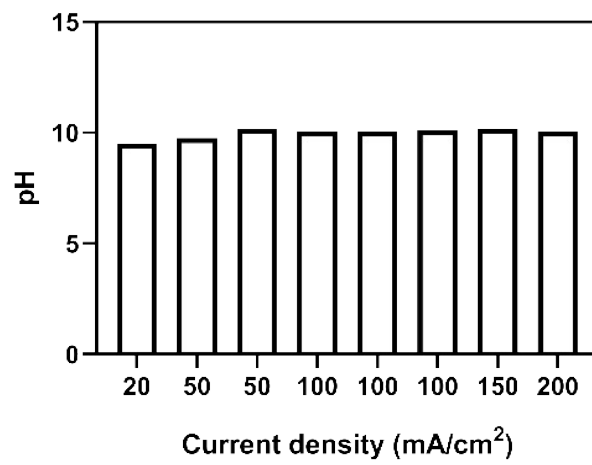


Fig. S22 The pH value of the catholyte after electrolysis at varied current densities.

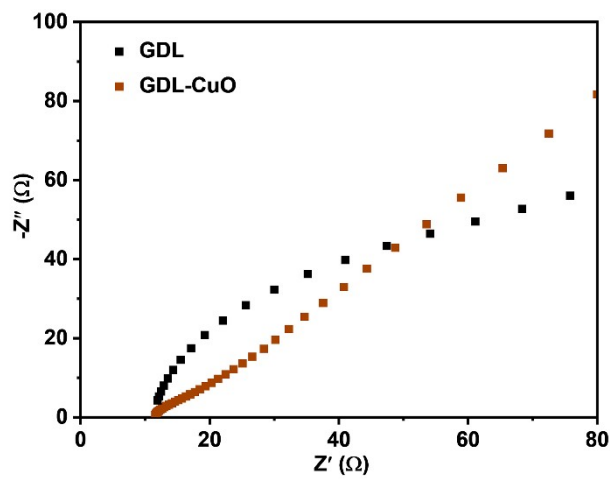


Fig. S23 Nyquist plots.

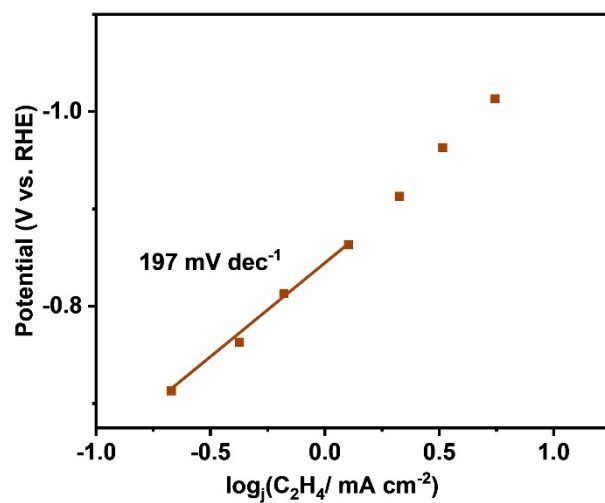


Fig. S24 Tafel curves for ethylene formation in 0.1 M KCl.

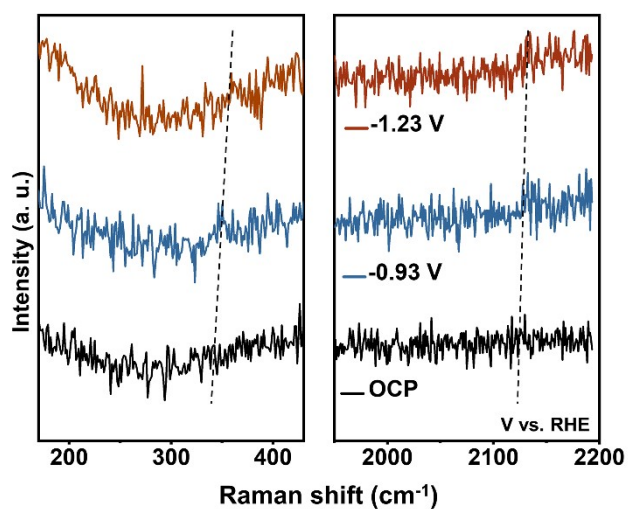


Fig. S25 Operando Raman spectroscopy of Cu electrocatalysts/GDL during electrochemical reduction of CO₂ in 0.1 M KCl.

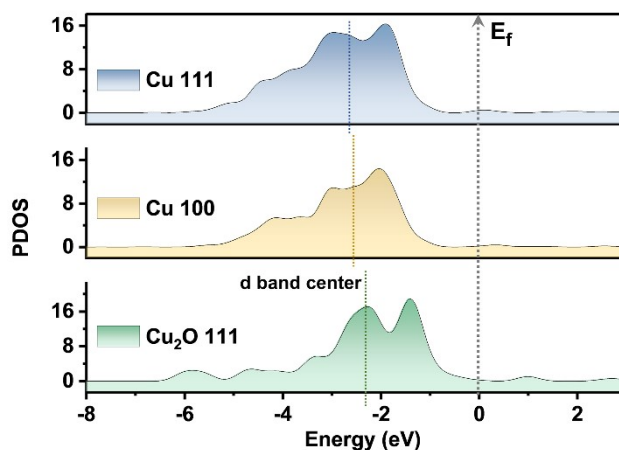


Fig. S26 d-band centers.

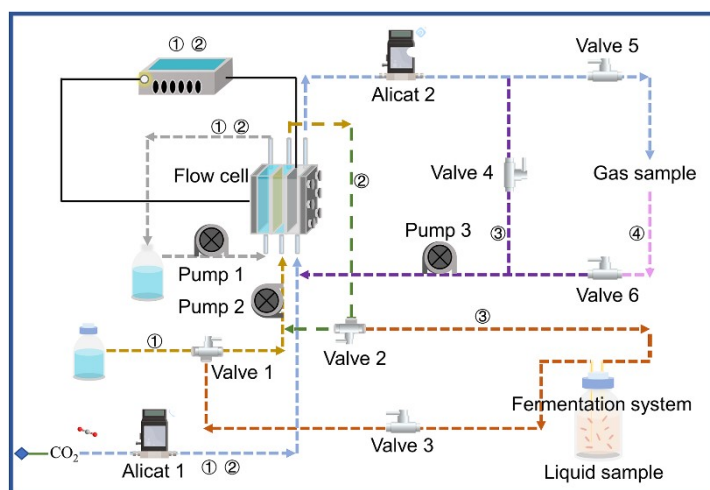


Fig. S27 Schematic diagram of the tandem experiment. The gray dotted line indicates the flow of the analyte. The blue, purple, and pink dotted lines indicate the flow of gases, including CO_2 and the produced gaseous products. The brown, green, and red dotted lines indicate the flow of the catholyte. The nearby serial numbers indicate the electrochemical workstations or lines involved in different stages. The first stage was designed to test the performance and stability of the catalyst. The catholyte flowed in and out (brown) under a constant current density of 100 mA/cm^2 , and the gas was analyzed by GC (blue). When the stability was confirmed, the

catholyte was cycled in the second stage (green). The electrolysis was kept for 10 minutes and stopped before the third stage. Immediately, the gas was sealed and cycled, passing through the gas chamber slowly (purple). The medium with bacteria was introduced and cycled in the meantime (red). Finally, when the metabolic process was finished, the gas was extruded into the GC for testing (pink).



Fig. S28 A photograph of the electro-bio reactor and the experimental setup. (The three-way valve replaced the valve 1, 2 and 3)

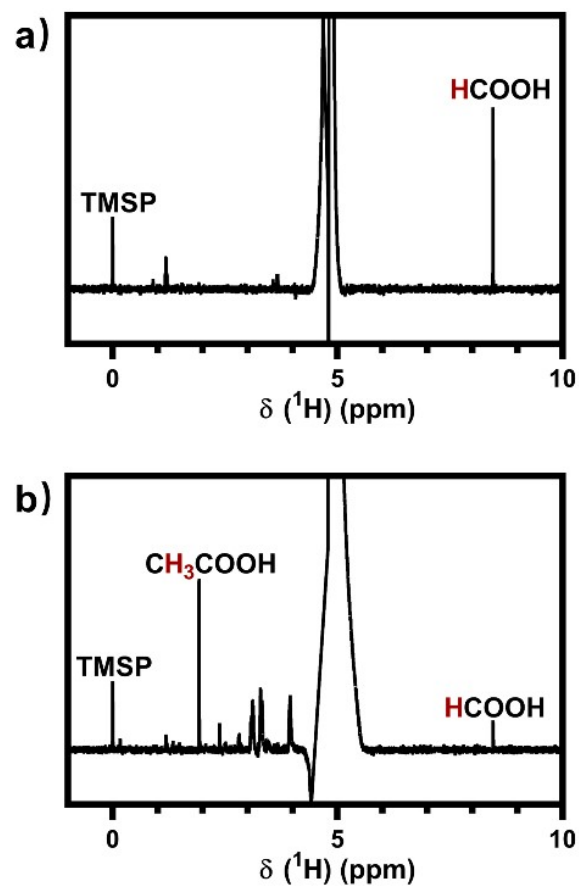


Fig. S29 The ^1H -NMR spectra of the catholyte before (a) and after (b) the tandem experiments.

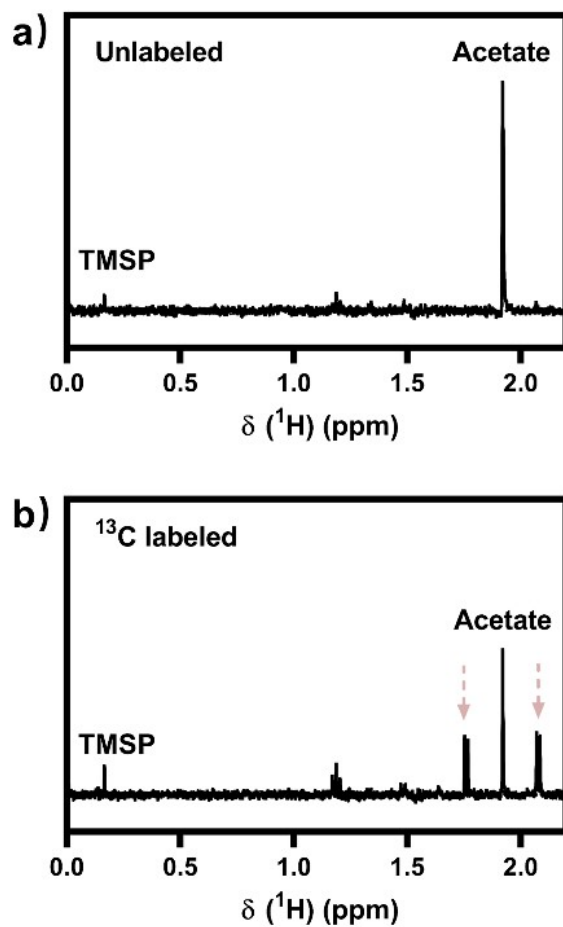


Fig. S30 ^1H -NMR spectra of acetate labeled with ^{13}C . For the ^{13}C -labeled samples, the high abundance of ^{13}C in the acetate magnifies $^1J_{\text{CH}}$ coupling, resulting in satellite peaks in the ^1H -NMR spectrum. The unlabeled sample shows a single peak with a 1.92 ppm chemical shift.

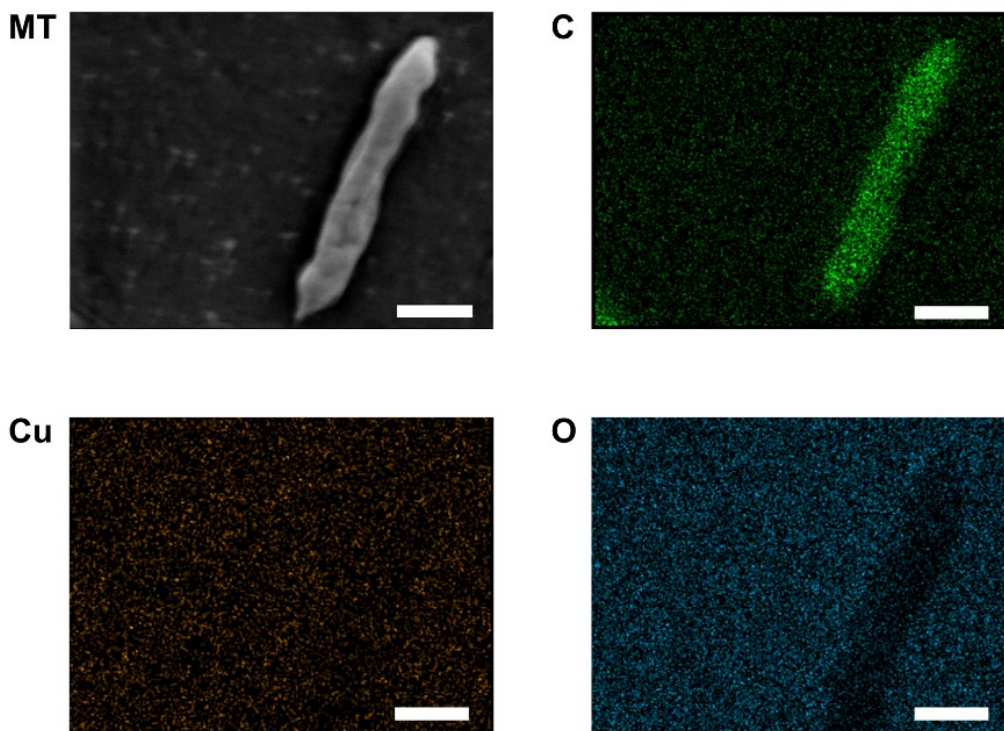


Fig. S31 The bacteria in the medium were collected after the tandem experiments. a) SEM image and EDX maps of the microbe showing uniform C distribution without copper ion accumulation. All scale bars are 500 nm.

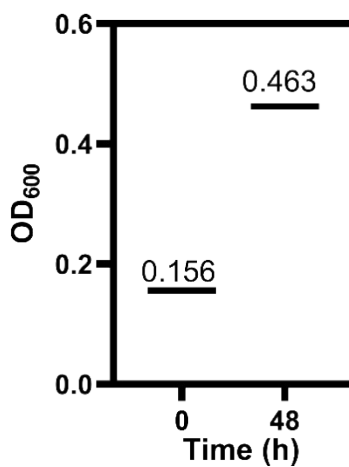


Fig. S32 The OD₆₀₀ of *M. thermoacetica* in media after 48 hours of proliferation with 8 g.L⁻¹ glucose as energy and carbon sources, containing an initial inoculum of bacteria taken out from the 12-hour tandem experiment.

2. Supplementary Tables

Moorella thermoacetica ATCC39073 was obtained from the Global Bioresource Center ATCC.

The defined medium, undefined medium, and heterotrophic medium were prepared in deionized water as follows:

Table S1. Medium

Component	Defined medium (g L ⁻¹)	Undefined medium (g L ⁻¹)	Heterotrophic medium (g L ⁻¹)
<i>Salt Mix:</i>			
NH ₄ Cl	0.5	0.5	0.5
MgCl ₂ ·6H ₂ O	0.18	0.18	0.18
<i>Buffer:</i>			
KH ₂ PO ₄	1.5	1.5	1.5
Na ₂ HPO ₄ ·12H ₂ O	4.2	4.2	4.2
NaOH (CO ₂)	8	8	8
<i>Indicator:</i>			
Resazurin (0.1%)	1 mL	1 mL	1 mL
<i>Reductant:</i>			
Na ₂ S·9H ₂ O	0.5	0.5	0.5
L-Cysteine·HCl	0.5	0.5	0.5
<i>Supplemental Components:</i>			
Vitamin Solution ^{a)}	0.5 mL	0.5 mL	0.5 mL
Wolfe's Modified Mineral Elixir ^{b)}	5 mL	5 mL	5 mL
Yeast Extract	0	1	2
Glucose	0	0	8

Table S2. Vitamin solution

Vitamin Solution ^{a)}	Concentration (g L ⁻¹)
Biotin	0.01
p-Aminobenzoic acid	0.025
Folic acid	0.01
Pantothenic acid calcium salt	0.025
Nicotinic acid	0.025
Vitamin B ₁₂	0.001
Thiamine·HCl	0.005
Pyridoxine hydrochloride	0.1
Thioctic acid	0.025
Riboflavin	0.005

Table S3. Mineral solution.

Wolfe's Modified Mineral Elixir ^{b)}	Concentration [g L ⁻¹]
Nitrilotriacetic acid	1.5
MgSO ₄ ·7H ₂ O	3.0
MnSO ₄ ·H ₂ O	0.5
NaCl	1.0
FeSO ₄ ·7H ₂ O	0.1
Co(NO ₃) ₂ ·6H ₂ O	0.1
CaCl ₂ (anhydrous)	0.1
ZnSO ₄ ·7H ₂ O	0.1
CuSO ₄ ·5H ₂ O	0.01
AlK(SO ₄) ₂ (anhydrous)	0.01
Boric acid	0.01
Na ₂ MoO ₄ ·2H ₂ O	0.01
Na ₂ SeO ₃ (anhydrous)	0.001
NiCl ₂ ·6H ₂ O	0.04
Na ₂ WO ₄	0.04

Table S4. Faradaic efficiency (FE) and Faradaic selectivity (FS) of acetate in liquid products.

(Orange shading: MES; blue shading: Cu-based ECR)

Bio/Electrocatalyst	pH	Electrolyte	Concentration [mol L ⁻¹]	FE _{acetate} %	FS _{acetate} %	Ref.
<i>M. thermoacetica</i>	7	Medium	0.1	80	100	[3]
<i>M. thermoacetica</i>	7	Medium	0.05	79	100	[4]
<i>S. ovata</i>	7	Medium	0.03	76.2	88.6	[5]
<i>S. ovata</i>	7	Medium	0.03	86	100	[6]
<i>R. eutropha</i> + In foil	7	Medium	0.1	0	0	[7]
<i>C. autoethanogenum</i> + <i>kluveri</i> + Ag	6	Medium	0.04	0.03	94.2	[8]
<i>S. ovata</i> + Co-P alloy	7	Medium	0.2	99	100	[9]
mixed wild-type+ Cu foil	7	Medium	0.07	—	—	[10]
mixed wild-type	7	Medium	0.06	58	100	[11]
mixed wild-type	7	Medium	0.06	61	100	[12]
Cu NPs@CNTs	7.8	KHCO ₃	0.5	1.69	56.3	[13]
Cu-CuO	7	KCl	0.1	48.5	60.1	[14]
Cu(B)	7	KCl	0.1	0	0	[15]
Cu(N)	6.8	KHCO ₃	0.1	0	0	[16]
100-cycled Cu nanocube	7	KHCO ₃	0.25	0	0	[17]
Cu-fragment	6.8	KHCO ₃	0.1	2	10	[18]
Cu ₄ Zn	6.8	KHCO ₃	0.1	1.0	2.4	[19]
Au/Cu	6.8	KHCO ₃	0.1	0.3	1.8	[20]
Ag/Cu	6.8	KHCO ₃	0.1	0	0	[21]
CuAg	6.8	KHCO ₃	0.1	0	0	[22]
CuAg	6.9	KHCO ₃	0.2	0	0	[23]
PTF(Ni)/Cu	6.8	KHCO ₃ /KCl	0.1	0	0	[24]
<i>M. thermoacetica</i> +Cu	7	KCl+medium	0.1	43.7	79.6	This work

c) Additional hydrogen was used; thus, the faradaic efficiency could not be calculated.

Table S5. Rate of electron conversion to products (v_e , unit: mmol h⁻¹ m⁻²) by microbial electrosynthesis (MES), Cu-based electrochemical CO₂ reduction (Cu ECR), tandem

electrochemical CO₂ reduction (tandem Cu ECR) in a neutral electrolyte. (Orange shading: MES; blue shading: Cu-based ECR)

Bio/Electrocatalyst	pH	V _{eC₂H₄}	V _{eCH₃COOH}	V _{eC₂H₅OH}	V _{C₃}	V _{C₄+}	V _{et total^{d)}}	Ref.
<i>M. thermoacetica</i>	7	0	0.5	0	0		0.5	[3]
<i>M. thermoacetica</i>	7	0	0.7	0	0		0.7	[4]
<i>S. ovata</i>	7	0	65.1	0	0		65.1	[5]
<i>S. ovata</i>	7	0	15.3	0	0		15.3	[6]
<i>R. eutropha</i> + In foil	7	0	0	0	0	204.5	204.5	[7]
<i>C. autoethanogenum</i> + Ag	6	0	6480	420	0		6900	[8]
<i>S. ovata</i> + Co-P alloy	7	0	743.1	0	0		743.1	[9]
mixed wild-type+ Cu foil	7	0	20.4	0	0		20.4	[10]
mixed wild-type	7	0	105.4	0	0		105.4	[11]
mixed wild-type	7	0	135.8	0	0		135.8	[12]
Cu NPs@CNTs	7.8	0	105.0	0	0		105.0	[13]
Cu-CuO	7	0	2080.7	1351.4	0		3432.1	[14]
Cu(B)	7	13579.3	0	7050.8	0		20630.1	[15]
Cu(N)	6.8	3182.6	0	1550.5	489.6		5222.8	[16]
100-cycled Cu nanocube	7	8117.7	0	3297.8	3805.2		15220.7	[17]
Cu-fragment	6.8	1817.0	0	761.0	0		2578.0	[18]
Cu ₄ Zn	6.8	328.8	29.4	890.2	201.4		1449.8	[19]
Au/Cu	6.8	376.7	8.2	177.4	215.8		778.1	[20]
Ag/Cu	6.8	309.6	0	0	0		309.6	[21]
CuAg	6.8	1389.6	0	1538.9	0		2928.5	[22]
CuAg	6.9	611.2	0	0	0		611.2	[23]
PTF(Ni)/Cu	6.8	1156.5	0	0	0		1156.5	[24]
<i>M. thermoacetica</i>+Cu	7	7912.5	201.2	0	0		8113.8	This work

d) The rate of electron conversion is for all C₂₊ products.

References

- 1 S. J. Clark, M. D. Segall, C. J. Pickard, P. J. Hasnip, M. I. J. Probert, K. Refson, M. C. Payne, Z. Kristallogr. - Cryst. Mater. 2005, **220**, 567.
- 2 J. P. Perdew, K. Burke, M. Ernzerhof, Phys. Rev. Lett. 1996, **77**, 3865.
- 3 K. P. Nevin, S. A. Hensley, A. E. Franks, Z. M. Summers, J. Ou, T. L. Woodard, O. L. Snoeyenbos-West, D. R. Lovley, Appl. Environ. Microbiol. 2011, **77**, 2882.
- 4 N. Faraghiparapari, K. Zengler, J. Chem. Technol. Biotechnol. 2017, **92**, 375.
- 5 K. P. Nevin, T. L. Woodard, A. E. Franks, Z. M. Summers, D. R. Lovley, mBio 2010, **1**, e00103.
- 6 T. Zhang, H. Nie, T. S. Bain, H. Lu, M. Cui, O. L. Snoeyenbos-West, A. E. Franks, K. P. Nevin, T. P. Russell, D. R. Lovley, Energy Env. Sci 2013, **6**, 217.
- 7 H. Li, P. H. Opgenorth, D. G. Wernick, S. Rogers, T.-Y. Wu, W. Higashide, P. Malati, Y.-X. Huo, K. M. Cho, J. C. Liao, Science 2012, **335**, 1596.
- 8 T. Haas, R. Krause, R. Weber, M. Demler, G. Schmid, Nat. Catal. 2018, **1**, 32.
- 9 R. M. Rodrigues, X. Guan, J. A. Iñiguez, D. A. Estabrook, J. O. Chapman, S. Huang, E. M. Sletten, C. Liu, Nat. Catal. 2019, **2**, 407.
- 10 K. Chatzipanagiotou, L. Jourdin, C. J. N. Buisman, D. P. B. T. B. Strik, J. H. Bitter, ChemCatChem 2020, **12**, 3900.
- 11 S. A. Patil, J. B. A. Arends, I. Vanwonterghem, J. van Meerbergen, K. Guo, G. W. Tyson, K. Rabaey, Environ. Sci. Technol. 2015, **49**, 8833.
- 12 S. Gildemyn, K. Verbeeck, R. Slabbinck, S. J. Andersen, A. PrévotEAU, K. Rabaey, Environ. Sci. Technol. Lett. 2015, **2**, 325.
- 13 C. Genovese, C. Ampelli, S. Perathoner, G. Centi, Green Chem. 2017, **19**, 2406.
- 14 Q. Zhu, X. Sun, D. Yang, J. Ma, X. Kang, L. Zheng, J. Zhang, Z. Wu, B. Han, Nat. Commun. 2019, **10**, 3851.

- 15 Y. Zhou, F. Che, M. Liu, C. Zou, Z. Liang, P. De Luna, H. Yuan, J. Li, Z. Wang, H. Xie, H. Li, P. Chen, E. Bladt, R. Quintero-Bermudez, T.-K. Sham, S. Bals, J. Hofkens, D. Sinton, G. Chen, E. H. Sargent, *Nat. Chem.* 2018, 10, 974.
- 16 Z.-Q. Liang, T.-T. Zhuang, A. Seifitokaldani, J. Li, C.-W. Huang, C.-S. Tan, Y. Li, P. De Luna, C. T. Dinh, Y. Hu, Q. Xiao, P.-L. Hsieh, Y. Wang, F. Li, R. Quintero-Bermudez, Y. Zhou, P. Chen, Y. Pang, S.-C. Lo, L.-J. Chen, H. Tan, Z. Xu, S. Zhao, D. Sinton, E. H. Sargent, *Nat. Commun.* 2018, 9, 3828.
- 17 K. Jiang, R. B. Sandberg, A. J. Akey, X. Liu, D. C. Bell, J. K. Nørskov, K. Chan, H. Wang, *Nat. Catal.* 2018, 1, 111.
- 18 H. Jung, S. Y. Lee, C. W. Lee, M. K. Cho, D. H. Won, C. Kim, H.-S. Oh, B. K. Min, Y. J. Hwang, *J. Am. Chem. Soc.* 2019, 141, 4624.
- 19 D. Ren, B. S.-H. Ang, B. S. Yeo, *ACS Catal.* 2016, 6, 8239.
- 20 C. G. Morales-Guio, E. R. Cave, S. A. Nitopi, J. T. Feaster, L. Wang, K. P. Kuhl, A. Jackson, N. C. Johnson, D. N. Abram, T. Hatsukade, C. Hahn, T. F. Jaramillo, *Nat. Catal.* 2018, 1, 764.
- 21 H. Zhang, X. Chang, J. G. Chen, W. A. Goddard, B. Xu, M.-J. Cheng, Q. Lu, *Nat. Commun.* 2019, 10, 3340.
- 22 L. R. L. Ting, O. Piqué, S. Y. Lim, M. Tanhaei, F. Calle-Vallejo, B. S. Yeo, *ACS Catal.* 2020, 10, 4059.
- 23 Y. Liu, H. Qiu, J. Li, L. Guo, J. W. Ager, *ACS Appl. Mater. Interfaces* 2021, 13, 40513.
- 24 D. Meng, M. Zhang, D. Si, M. Mao, Y. Hou, Y. Huang, R. Cao, *Angew. Chem.* 2021, 133, 25689.